Flow and mixing in Ascension, a steep, narrow canyon

M.C. Gregg,[1] R.A. Hall,[2] G.S. Carter,[2] M.H. Alford,[1] R.-C. Lien,[1] D.P. Winkel,[1] and D.J. Wain[1]

[1]Applied Physics Laboratory, University of Washington, 1013 NE 40th Street, Seattle, WA, 98105 USA

[2]Department of Oceanography, University of Hawai'i at Manoa, 1000 Pope Road, Honolulu, HI, 96822 USA

Abstract. A thin gash in the continental slope northwest of Monterey Bay, Ascension Canyon is steep, with sides and axis both strongly supercritical to M_2 internal tides. A hydrostatic model forced with eight tidal constituents shows no major sources feeding energy into the canyon, but significant energy is exchanged between barotropic and baroclinic flows along the tops of the sides, where slopes are critical. Average turbulent dissipation rates observed near spring tide during April are half as large as a two-week average measured during August in Monterey Canyon. Owing to Ascension's weaker stratification, however, its average diapycnal diffusivity, 3.9×10^{-3} m^2 s^{-1}, exceeded the 2.5×10^{-3} m^2 s^{-1} found in Monterey. Most of the dissipation occurred near the bottom, apparently associated with an internal bore, and just below the rim, where sustained cross-canyon flow may have been generating lee waves or rotors. The near-bottom mixing decreased sharply around Ascension's one bend, as did vertically integrated baroclinic energy fluxes. Dissipation had a minor effect on energetics, which were controlled by flux divergences and convergences and temporal changes in energy density. In Ascension, the observed dissipation rate near spring tide was 2.1 times that predicted from a simulation using eight tidal constituents averaged over a fortnightly period. The same observation was 1.5 times the average of an M_2-only prediction. In Monterey, the previous observed average was 4.9 times the average of an M_2-only prediction.

1. Introduction

1.1. Background

Because submarine canyons are major bathymetric features on most continental shelves and slopes, the unique processes in and around them are inherently significant components of coastal dynamics. Current efforts to understand internal waves and mixing in canyons began in the 1970s with discovery of intense internal waves in canyons on opposite U.S. coasts. Analyzing moored current meters in La Jolla Canyon, California, *Gordon and Marshall* [1979] noted elevated internal waves and attributed them to trapped waves reflecting from the side walls. *Wunsch and Webb* [1979], comparing internal wave intensities in deep ocean mooring data, reported that the highest internal wave energies were in Hydrographer Canyon, on the edge of the continental shelf southeast of Nantucket Island. Subsequently, CTD profiles and five moorings in Hudson Canyon, a seaward extension of the Hudson River, revealed that spectral densities increased toward the canyon's head, consistent with shoreward phase propagation between the moorings [*Hotchkiss and Wunsch*, 1982]. Volume-integrated horizontal kinetic energy, *hke*, was 0.35 MJ, about one-third of the 1.0 MJ of potential energy, *pe*. Baroclinic energy transport into the canyon was crudely estimated from the *Garrett and Munk* [1975] internal wave spectrum by evaluating expressions for p', w', and u', assuming their correlations, and integrating across top and seaward faces, yielding about 2.5 MW, ten times that attributed to near-bottom dissipation by an oscillating boundary layer flow.

During August 1997, intensive measurements were made in Monterey Canyon: microstructure profiles at the shallow end [*Carter and Gregg*, 2002] (referred to hereinafter as MC97), Expendable Current Profilers (XCPs) near the entrance [*Kunze et al.*, 2002], and two moorings in the upper canyon [*Key*, 1999]. After *Gregg et al.* [2005] corrected a calibration error, $\overline{\epsilon} = 1.97 \times 10^{-7}$ W kg^{-1} within 8 km of the canyon head, with a corresponding diapycnal diffusivity of $K_\rho \equiv 0.2\overline{\epsilon}\ \overline{N^{-2}} = 2.5 \times 10^{-3}$ m^2 s^{-1}. (K_ρ for each profile was computed using N^2 from the observed density profile after it was resorted to be monotonic). Mixing was strongest over the canyon's axis and larger during spring than during neap tides. These levels were much larger than predicted from finescale mixing parameterizations, leading *Kunze et al.* [2002] to suggest that scattering off side walls may generate turbulence more efficiently than open ocean wave–wave interactions. At least part of the near-bottom turbulence was produced by strong, up-canyon bores, nearly phase locked to the surface tide, arriving at the measurement site about 8.6 hours after high water at the Monterey pier [*Key*, 1999].

Frequency spectra of velocity from an acoustic Doppler current profiler (ADCP), moored where the thalweg was 300–400 m deep, had peaks at tidal frequencies of K_1, M_2, M_4, M_6, and M_8 [*Key*, 1999]. No peak was evident at the near-inertial frequency, f; nor was one expected, owing to suppression of nearly circular horizontal motions by the side walls. The ratio of *hke* to *pe* was 2.06–2.10, compared to the theoretical ratio of 2.13 for M_2 internal tides [*Fofonoff*, 1969]. The vertically integrated energy flux into the canyon was 5 kW m^{-1}, decreasing landward, most rapidly around some sharp bends, until it reached ± 1 kW m^{-1} near the shallow end [*Kunze et al.*, 2002]. Consistent with dominance by low modes, flux magnitudes were minimal at mid-depths. Flux convergences and divergences along the canyon were always significantly larger than ϵ, most likely reflecting generation of the internal tide and conversion from baroclinic to barotropic energy within the canyon, in addition to possible underestimation of dissipation rates owing to limited spatial coverage.

Within 8 km of the head, *pe* decreased while *hke* decreased and then increased. Contrary to inferences by *Hotchkiss and Wunsch* [1982], no evidence was found for ϵ or K_ρ increasing toward the head.

On Taiwan's south coast, Kaoping Canyon, similar to Monterey Canyon in size, also begins close to shore and meanders seaward around sharp bends. At the seaward side of the major bend, flux of the internal tide is $\approx 14\ \mathrm{kW\,m^{-1}}$ [*Lee et al.*, 2009b], five times that at a comparable location in Monterey. Spectra of currents had strong K_1 and M_2 peaks and some harmonics. K_ρ, estimated from density overturns, is $\approx 10^{-2}\,\mathrm{m^2\ s^{-1}}$ [*Lee et al.*, 2009a].

Applying the Princeton Ocean Model (POM) to generation and propagation of internal tides in an idealized canyon, *Petruncio et al.* [2002] report energy of the internal tide concentrated on the south side, which they attribute to the earth's rotation. Small changes in bottom slope along the thalweg, or deepest path, greatly affected energy of the internal tide, but subcritical slopes produced little baroclinic energy. Near-critical slopes had strong internal tides propagating shoreward, and canyons near-critical at their mouths and supercritical within generated internal tides most effectively.

Jachec et al. [2006] applied the Stanford Unstructured Nonhydrostatic Terrain-following Adaptive Navier–Stokes Simulator (SUNTANS) over 100 km in latitude, encompassing all of Monterey Bay and its environs. Sur Platform, a broad rise to depths of 1,000 m off Pt. Sur, was found to be the major source for M_2 energy, much of which followed bathymetric contours into Monterey Canyon. Using POM over a wider region, *Carter* [2010] reports additional M_2 sources, concluding that larger domains with accurate bathymetry are more important than non-hydrostatic flow in simulating the internal tide. *Hall and Carter*

[2010] examined the results of the POM run in Monterey Canyon, finding that the internal tide is topographically steered around the canyon's bends. Laterally strongest along the axis, maximum vertically-integrated baroclinic energy fluxes began as 1.5 $\mathrm{kW\,m^{-1}}$ at the mouth of the upper canyon and peaked at > 4 $\mathrm{kW\,m^{-1}}$ around the first large bends, evidence of strong internal tide generation within the canyon. Most intense at the bottom, the laterally-integrated along-canyon energy flux decreased monotonically from 9 MW at the mouth to 1 MW at the Gooseneck Meander.

1.2. Motivation and outline

During a return to Monterey Canyon in April 2009, we took limited measurements in nearby Ascension Canyon to investigate our hypothesis that mixing in a short, relatively straight, steep, and narrow canyon is significantly less than in Monterey, also assuming that Ascension lacks offshore internal tide sources as strong as those feeding energy into Monterey. After examining bathymetry in Section 2 and describing the observations in Section 3, several POM runs are discussed in Section 4, including those without the canyon in the bathymetry. In addition, observations with an Acoustic Doppler Current Profiler (ADCP) at the canyon head are compared with model predictions. Observed mixing averages, patterns, and processes are examined in Section 5, followed by baroclinic fluxes and a rough energy balance in Section 6. A summary and discussion in Section 7 conclude the presentation.

2. Bathymetry

Cutting through the continental slope at the northwest corner of Monterey Bay (Figure 1), Ascension lies in a cluster of three canyons 12 km from the coast. Its nearest neighbor, Ano Nuevo Canyon, lies only a few kilometers east (Figure 2). Around the head of the canyon, the shelf is flat and 120 m deep. We reference distance along the thalweg, or deepest path, from the 200-m isobath, where the canyon is a shallow bowl. Three kilometers to seaward, the channel turns clockwise and narrows to 0.5 km, flanked by sides having slopes $\gamma \geq 1$. Past 4 km, the canyon's rim descends along the continental slope, and at 8 km the upper sides widen, blending smoothly into the surrounding slope at their tops. Table 1 includes characteristics of Ascension and Monterey canyons.

Along the upper canyon, the thalweg descends 700 m in 9 km, with slopes of 0.03 to 0.2, averaging 0.078, or 4.5° (Figure 3). To interpret some of the measurements, two rim depths are used. The upper is 2 km horizontally from the thalweg, where the bottom begins sloping into the canyon, and the lower is where slopes into the canyon first exceed 0.25. Cross-sectional area between the upper rims decreases from $\approx 3\,\mathrm{km}^2$ at 9 km to $\approx 0.5\,\mathrm{km}^2$ at 2 km.

M_2 internal tides entering upper Monterey Canyon should scatter forward, toward the canyon's head, because its thalweg slope is less than the critical frequency, $\omega_c = \sqrt{(f^2 + \gamma^2 N^2)/(\gamma^2 + 1)}$, evaluated for ω_{M_2} [*Carter and Gregg*, 2002], where f and N are the inertial and buoyancy frequencies. By contrast, most of the Ascension thalweg is strongly supercritical, i.e., $\omega_c > \omega_{\mathrm{M}_2}$ (Figure 3, upper), reflecting M_2 internal tides back to seaward. Because the internal wave energy spectrum is 'red', $\propto \omega^{-2}$, only the high-frequency, low-energy part of the internal wave continuum spectrum can scatter toward the head. Some places, however, have $\omega_{\mathrm{K}_1} < \omega_c < \omega_{\mathrm{M}_2}$ and could be sites for generating internal tides within the canyon.

Cross-canyon slopes as large as 2 (Figure 3, upper) exceed those of Monterey. Over much of the upper canyon, the central slope minimum defining the thalweg is barely 100 m across and never more than 500 m. The Rossby radius for internal mode i is $Ro_i = c_i/f$, where c_i is the wave speed, obtained by solving the extended Taylor–Goldstein equation [*Pratt et al.*, 2000] for internal waves in the canyon. Mode-one values range from 2.3 to 8.6 km between 1.5 and 6 km on the thalweg, much greater than the canyon's width, and those for mode-three are 1.7 to 3.5 km, also indicating that rotation is not dynamically important even for these modes.

Though steeper than other places we have sampled, the cross-canyon profiles are close to a negative 'Witch of Agnesi' shape, $z = h_{\mathrm{m}}/(1 + (x/a)^2)$, e.g., with $h_{\mathrm{m}} = 413$ m and $a = 375$ m at 4 km. Collecting cross-canyon data was beyond the scope of these observations, and would not have succeeded, owing to the minimum speeds needed to maintain steerage in rough seas.

3. Observations

Working from R/V *Wecoma*, on 13 April (yday 102.9) we placed a 300-kHz WorkHorse ADCP at the canyon's head (37.0245°N, 122.4089°W) in 198 m of water (yday are defined as starting with 0.0 at midnight December 31, 2008). After setting the mooring, we began microstructure profiling, taking AMP (Advanced Microstructure Profiler) group 5 along the thalweg near spring tide. Ascension, however, is exposed to north Pacific swell, unlike upper Monterey Canyon, and rising winds and seas forced us to stop after 15 hours and 16 profiles.

After finishing in Monterey Canyon on 25 April, we returned to Ascension to sample near the next spring tide, intending alternate runs along the canyon with AMP and

SWIMS3, a depth-cycling towed body carrying 300-kHz WorkHorse ADCPs looking upward and downward, a 911+ Sea-Bird CTD, and fluorescence, for chlorophyll. Most SWIMS3 runs were made at ship speeds of ≈ 1.5 kts, and the towed body descended and rose at ≈ 1 m s^{-1}, giving profiles an aspect ratio of about 1:1 AMP and SWIMS3 data were organized into groups and subs. Data with one objective, e.g., sampling Ascension during one period of the diurnal tide, are termed groups, and individual runs, in one direction in the case of Ascension, are termed subs.

Because winds and seas were again rising and time was limited, we recovered the WorkHorse at yday 114.6 before beginning intensive sampling of the canyon with SWIMS3 and AMP. A single profile was formed for each descent and ascent of the towed body, using 8-m bins for ADCP records. Acoustic altimeters permitted close approaches to the bottom with both instruments, but, to limit depth-cycle times, SWIMS3 did not go below 650 m. Consequently, past thalweg distances of 5.5 km SWIMS3 profiles ended at increasing distances above the bottom, 225 m by 9 km. To allow adequate sampling of the central part of the canyon, no runs began at thalweg distances less than 1 km. Figure 4 shows distances and times of profiles and the duration of each transect, termed a sub. After a day of mostly SWIMS runs, *Wecoma's* stern was heaving the towed body so badly that we recovered it and resumed using AMP. In all, SWIMS group 18 contained 140 profiles, and AMP group 7 had 21.

Dissipation rates were measured directly with two airfoils on AMP, and, following *Thorpe* [1977], were inferred for SWIMS3 profiles from density overturns by inverting Ozmidov's relation [*Ozmidov*, 1965], following *Dillon* [1982], to give $\epsilon = 0.64 l^2 N^3$, where l is the root-mean square (RMS) overturning length, and N across the overturn was obtained after sorting the profiles to increase monotonically. Detectable overturns were ≈ 0.5 m and larger.

4. Numerical predictions

A modified version of the Princeton Ocean Model (POM) was used to estimate surface and internal tides incident on Ascension Canyon. Following *Carter* [2010] and *Hall and Carter* [2010], the domain extended from 123° 43′ 59″W, 35° 31′ 13″N to 121° 44′ 8″W, 37° 9′ 50″N, had 250-m horizontal resolution, and 51 sigma levels evenly spaced in the vertical. Stratification was specified using average temperature and salinity profiles from a 12-hour CTD time series (7 profiles) taken 18–19 February 2009 at 123° 00′ 00″W, 36° 36′ 30″N.

The model was forced along the boundaries with eight tidal constituents (M_2, S_2, N_2, K_2, K_1, O_1, P_1, and Q_1) from the West Coast and California TPXO6.2 inverse model [*Egbert*, 1997; *Egbert and Erofeeva*, 2002]. M_2 contributed three times as much variance as K_1. Due to storage limitations, time-series output were not saved for the entire domain; rather, 'virtual moorings' were placed at the WorkHorse location and in a grid over Ascension Canyon. The model was output to the virtual moorings every 320 s between yday 102.0 and 117.0.

4.1. Comparison of model and observations

Tidal heights, h, observed with the WorkHorse mooring are compared to the model and to sea level observed at Monterey pier (Figure 5, upper). RMS height differences between the Ascension WorkHorse and Monterey pier averaged 54 mm when WorkHorse heights were positive and 64 mm when they were negative. Because the WorkHorse record is too short to determining zero displacement accurately, apparent biases may not be real. RMS differences between the model and the WorkHorse were 53 and 40 mm during positive and negative displacements. Comparing spectral amplitudes (Figure 5, middle) shows little difference in the semi-diurnal (dominated by M_2) and diurnal (dominated by K_1) band magnitudes. The record length is much too short to distinguish S_2 from M_2 or O_1 from K_1. Not surprisingly, coherence-squared is unity and relative phase is zero over the range of the forcing frequencies. There is no evidence of inertial oscillations in these data.

Nearly along-canyon, observed north/south velocities, v, have a relatively symmetric histogram (not shown) and are approximately twice those modeled ($-0.30 \lesssim v_{obs} \lesssim 0.30$ m s^{-1} compared to $0.14 \lesssim v_{model} \lesssim 0.14$ m s^{-1}). Observed east/west velocities, u, nearly across-canyon, are also approximately twice predictions ($-0.22 \lesssim u_{obs} \lesssim 0.31$ m s^{-1} compared to $0.10 \lesssim u_{model} \lesssim 0.13$ m s^{-1}), but are skewed towards positive velocities (not shown).

Vertically-averaged spectra of observed baroclinic v velocities (Figure 6) have strong diurnal and semidiurnal peaks, dominated by K_1 and M_2, respectively, as well as a smaller peak at M_4 ($2M_2$). No significant peaks, however, occur in the u spectrum, which is so much smaller than the v spectrum that it makes little contribution to the total velocity spectrum. At higher frequencies, the total spectrum is slightly below the *Levine* [2002] model spectrum for shallow water internal waves with an energy level equivalent to *Garrett and Munk* [1975] and $j_* = 3$. The model spectrum peaks in the diurnal and semidiurnal bands, where it was forced, as well as at higher harmonics such as M_2+K_1, $2M_2$, $2M_2$+K_1, etc. Little energy is transferred to other (non-harmonic) frequencies, generating a spiky appearance. Model v spectral peaks are 3–4 times smaller than the observed spectrum, even though they cover the entire water column, but the WorkHorse data were below the upper rim. (Somewhat less than 100 m, the WorkHorse range extended only slightly above the canyon.) Observed diurnal and semidiurnal peaks in the u spectrum are much broader than those of the model, indicating strong smearing of those motions.

Although the horizontal resolution of this model (250 m) is high for a regional tidal model, Ascension Canyon is not well resolved. At the latitude of the WorkHorse mooring, the canyon, as defined by the 150-m isobath, is only 4 cells wide. This is likely a major reason for the model's poor skill at predicting velocity in Ascension compared to Monterey Canyon [*Carter*, 2010].

4.2. Effect of the canyon

To examine how the canyon perturbs barotropic tidal flows, two single-constituent runs (K_1-only and M_2-only, representing the diurnal and semidiurnal bands) were performed with and without Ascension Canyon in the bathymetry. Comparing the runs shows that the canyon reduced velocity magnitudes (Figure 7) and altered directions 90° or more by topographic steering, e.g., near the head on the western wall M_2 flow goes toward the southwest when the canyon is included and toward the northwest without it. Changes are negligible beyond ≈ 2 km from the canyon's axis.

4.3. Fluxes and dissipation rates

Vertically-integrated and horizontally-averaged fluxes across the 200-m isobath into Ascension Canyon from the eight-constituent run varied between $\approx 70\ \mathrm{W\,m^{-1}}$ at spring tide and $\approx 5\ \mathrm{W\,m^{-1}}$ at neap. Integrating across the canyon mouth yielded ≈ 250 kW at spring, nearly zero at neap, and a time average of 115 kW (Table 1). Integrating around the rim gave –39 kW, yielding a net convergence of 76 kW, computed as average energy fluxes, $< \mathbf{u}'\mathrm{p}' >$, across the mouth and across the 200-m isobath. Conversion of barotropic to baroclinic energy within the canyon was 72 kW, computed as the area integral of $< p'(-H) \times \mathbf{u} \cdot \nabla H >$. Assuming that all net energy into the canyon was dissipated, as well as the internal wave energy generated within by barotropic-to-baroclinic energy conversion, average dissipation rates were 27.1 $\mathrm{mW\,m^{-2}}$ at spring tide, 5.6 $\mathrm{mW\,m^{-2}}$ at neap, and 16.1 $\mathrm{mW\,m^{-2}}$ averaged over time, or 4.85×10^{-8} $\mathrm{W\,kg^{-1}}$ per unit mass.

Forcing Ascension with only the M_2 component reduced flux into the mouth to 65 kW (from 115 kW), but yielded the same flux convergence, 76 kW, because there was a net inward flux of +11 kW across the rim in contrast to –39 kW lost across the rim using eight constituents. In addition, using only M_2 doubled barotropic-to-baroclinic conversion to 158 kW (from 72 kW), indicating significant interference between modes within the canyon. Owing to the increase in conversion, the predicted dissipation rate was 58% higher for M_2-only versus eight-constituent runs.

In contrast, the M_2-only flux into the mouth of Monterey was 9,023 kW, 139 times that entering Ascension. Relative to the incoming flux, barotropic-to-baroclinic conversion was tiny, 50 kW, a consequence of it being nearly balanced by baroclinic-to-barotropic conversion. Dissipating the net of 7,622 kW over the greater volume of Monterey gives an average dissipation of 3.99×10^{-8} $\mathrm{W\,kg^{-1}}$, 57% of the comparable dissipation rate computed for Ascension.

The average of all dissipation rates observed in Ascension below the rim is 1.02×10^{-7} $\mathrm{W\,kg^{-1}}$ compared to 1.97×10^{-7} for Monterey (Table 1). The Ascension data suffer from being collected only near spring tide along the thalweg and are likely an overestimate on both counts. Spanning a fortnightly cycle, Monterey data were mostly taken along the thalweg but some observations were off it, and all came from the inner 20% of the canyon's length. Nonetheless, we consider observations and predictions to be surprisingly close.

5. Mixing rates and patterns

Although observed dissipation rates in Ascension are less than those in Monterey, the difference is modest and could have resulted from differences in sampling coverage, in time and space. Here, we examine vertical and along-canyon patterns in the mixing.

5.1. Profiles

To examine spatial patterns, SWIMS3 data from each sub were interpolated onto a 0.5-km grid with 5-m vertical bins. The average profiles of temperature, salinity, and density were nearly linear with depth, but $< \epsilon(z) >_t$ (Figure 8, upper) was surprisingly uniform, except below 625 m, where only a few samples were collected. At most depths, $< \epsilon(z) >_t$ was 5–10 times less than the MC97 average, confirming suspicions that turbulent dissipation in Ascension might be significantly weaker than in Monterey. Stratification, however, was also weaker (MC97 was in August compared to April in Ascension) causing diapycnal diffusivity, $\mathrm{K}_\rho = 0.2\epsilon/N^2$, to be close to MC97, generally within a factor of two and equal at some depths.

Averaged by height, temperature and salinity decreased approximately linearly to $h =$ 175 m, but the changes were small, altering N^2 by only a factor of two (Figure 8, lower). Exceeding N^2 by a factor of 50 near the bottom, shear squared (S^2) decreased rapidly to equal N^2 above 200 m. N^2 during MC97 was even more uniform with height and

5–10 times larger than in Ascension. In both canyons, $< \epsilon(h) >_t$ decreased roughly exponentially from the bottom, falling about 10-fold by a height of 200 m. Never exceeding MC97, in some places dissipation was 5 times smaller. K_ρ, however, was 10^{-3}–10^{-2} m^2 s^{-1} within 300 m of the bottom, equalling or exceeding MC97, except in the bottom 25 m.

More than 200 m above the bottom, average SWIMS3 dissipation rates slightly exceeded or equalled those of AMP group 5, taken during neap tide, and AMP group 7, interlaced with SWIMS3 sampling during spring tide (Figure 9). Below 200 m, AMP group 5 is smaller and group 7 is larger than the SWIMS3 average. Formed from seven times the number of profiles, the SWIMS3 average is the more accurate. Low mixing rates near the bottom are curious in view of the large excess shear there, but anomalies like this are not unexpected in averages of a few samples from different times and places.

5.2. Changes in time averages along the canyon

From $\approx 5 \times 10^{-8}$ W kg^{-1} between 3 and 4.5 km, vertically averaged dissipation rates decreased sharply around the bend toward the head (Figure 10), mimicing patterns reported for Monterey [*Kunze et al.*, 2002]. The decline to seaward was more gradual and may result solely from not taking SWIMS3 below 650 m where the bottom was deeper. Sub averages varied by one decade near the head and twice that at 8 km. The variations were not in unison along the canyon, indicating that dissipation patterns changed with time as well as position. Twice model predictions, vertical integrals (Figure 10c) were ≈ 50 mW m^{-2} seaward of 3 km and, not surprisingly, decreased steeply toward the head, suggesting that full-depth averages would have been dominated by the deep end of the canyon.

5.3. Depth-distance patterns

Dissipation rates were often $\geq 10^{-7}$ W kg^{-1} throughout the canyon and rose to 10^{-6} W kg^{-1} in several patches (Figure 11), the largest at the bottom between 2.5 and 5 km, and the others between upper and lower rims. Diapycnal diffusivity was $\geq 10^{-3}$ m^2 s^{-1} and exceeded 10^{-2} m^2 s^{-1} in the major patches, which occupied over half the canyon. Between these patches, ϵ and K_ρ were lower, but nevertheless 5–10 times those above the rim.

Beginning near 5 km and thinning as the thalweg wrapped around the bend, the lower patches lay in layers of high shear and stratification extending seaward from the bottom. An AMP profile near the seaward end of this region revealed intense turbulence in a 50-m-thick homogenous bottom boundary layer capped by 150 m of overturns in water stratified in the mean (Figure 12). Contours of SWIMS3 sub 1 (Figure 13), and of other subs not shown, reveal isopycnals pushed up along the bottom, rising over 100 m above their apparent equilibrium positions, suggesting bores similar to those observed by *Key* [1999] in Monterey. The strongest dissipation was just over the landward end of the bore. Consistent with up-canyon bottom flow, fluorometer values (lower right, Figure 13) show chlorophyll pushed up along the bottom. Oxygen contours are similar (Figure 14).

Much smaller than the near-bottom mixing patch, the upper mixing patches were in a weakly stratified layer lying between the depths of the inner and outer rims, following their downward slope to seaward.

Just above, persistent 0.05 to 0.2 m s^{-1} westward flow crossed the canyon. Peaking over the gentle shelf break 6-9 km from the head, the westward flow extended 50 m below the upper rim into the canyon. In the average section (Figure 11), the low-N layer was 100 m thick toward the head and thinned to seaward, ending near 6 km, beneath maximum westward flow. During sub 1, the layer continued to 8.5 km. An AMP profile caught an even thicker example, with ϵ between 10^{-6} and 10^{-5} W kg^{-1} over 200 m in a homogenous layer (Figure 15). With observations only along the thalweg, the origin of this well-mixed layer curving downward to seaward cannot be determined conclusively, but the most plausible explanation for the downward slope tracking that of the rim is that it resulted from mixing generated by the observed flow across the canyon, possibly as rotors generated where the flow separated from the east rim of the canyon. Tidal beams from the rim, however, cannot be excluded.

6. Fluxes and energetics

General baroclinic fluxes are evaluated to examine energetics, rather than M_2 baroclinic fluxes, because SWIMS3 sampling was too interrupted by microstructure profiling for harmonic analysis (Figure 4). Following *Klymak et al.* [2010], *Nash et al.* [2005], and *Kunze et al.* [2002], baroclinic velocity fluctuations were determined by subtracting the time average profile. Subtracting the vertical average from the fluctuations yielded baroclinic velocity fluctuations, $u'_{\rm bc}$. Baroclinic pressure fluctuations were obtained following the same procedure except that a linear fit versus depth was also subtracted to remove effects of barotropic flows over sloping bottoms [*Nash et al.*, 2006]. The baroclinic energy flux,

$$F_{\rm bc}(x,z,t) = \hat{u}'_{\rm bc}(x,z,t)p'_{\rm bc}(x,z,t) \tag{1}$$

has units of W m^{-2}, the hat indicating the along-canyon component. The example in Figure 16a is typical, revealing peak values of ± 3 W m^{-2} embedded in coherent flows stretching several kilometers along the canyon. Vertical integrals decrease toward the head, becoming negligible at 2 km (Figure 17e). Peak magnitudes are 1 kW m^{-1}.

Horizontal baroclinic kinetic energy density is $hke \equiv (\rho/2)({u'_{\rm bc}}^2 + {v'_{\rm bc}}^2)$, and available potential energy density is $pe \equiv (\rho/2)N^2\zeta^2$, where ζ^2 is isopycnal displacement variance. Full-depth averages of hke decreased more than twofold toward the head, but pe increased to a maximum at 3 km before falling sharply (Figure 17). The pe value was more variable during the subs than the hke, but some variations appear related, e.g., sub 6 with low pe and high hke. Seaward of 4 km, the observed energy ratio, hke/pe, matched the value expected for free, single waves with M$_2$ frequency (Figure 17, right), $hke/pe = (N^2 - \omega_{M_2}^2)(\omega_{M_2}^2 + f^2)/N^2(\omega_{M_2}^2 - f^2) \approx 2.2$ [*Fofonoff*, 1969]. *Kunze et al.* [2002] report a similar result in Monterey Canyon. Between 1.5 and 4 km, however, the observed ratio decreased well below the theoretical ratio as pe increased and hke decreased. The ratio was partially restored by the subsequent sharp decline of pe landward of 3 km. The dip occurred on the landward side of the 50° bend, suggesting that the bend may have increased displacements without affecting the broader velocity decrease.

The baroclinic energy balance,

$$\frac{dE}{dt} + \frac{dF}{dx} = P - \rho_0\epsilon \quad [\mathrm{W\ m^{-3}}] \tag{2}$$

is evaluated in Figure 18 for subs 4, 5, and 6 using vertical averages (left) and vertical integrals (right). Computed as the residual of the three measured terms, production, P, followed flux divergence, dF/dx, sometimes slightly modified by changes in energy density, dE/dt. Balances with vertical averages and vertical integrals are roughly similar. As expected from hke/ϵ ratios in Figure 10d, in most cases dissipation only weakly affected energetics. Patterns along the canyon varied greatly, ending during sub 6 with strong flux convergence to landward and strong divergence to seaward.

An energy budget for the upper canyon (defined as the area within the 200-m isobath and up-canyon of 7 km) was constructed from model output using a 25-hour moving window. The kinetic and potential energy tendency is calculated the same way as from the observations, then integrated vertically over the area of the upper canyon. Baroclinic energy flux divergence is calculated as the up-slope component of the depth-averaged energy flux, integrated along the 200-m isobath, minus the up-canyon energy flux integrated along an across-canyon section, 7 km from the canyon head. The production term is calculated as barotropic-to-baroclinic energy conversion, $\langle p'(-H) \cdot (\overline{\mathbf{u}} \cdot \nabla H) \rangle$ [*Niwa and Hibiya*, 2001], integrated over the area of the upper canyon. The final term, baroclinic energy dissipation, is taken to be the residual of the three computed terms.

Of the three computed terms in the energy budget, modeled baroclinic energy flux divergence varies most with the spring–neap cycle, turning negative (i.e., convergent) during springs and weakly positive during neaps (Figure 19). As expected, baroclinic energy production is largest during springs. Moreover, energy tendency, dE/dt, is negative during the transition from spring to neap tide and positive when returning to springs. This term, however, has negligible effect on the budget. Baroclinic energy dissipation is typically the largest term, in stark contrast to the observed energy budget, and varies by the same order as energy divergence. Expressing volume and tidal cycle averages, these results cannot be compared directly with the instantaneous observed balances from a fraction of a tidal cycle, but the discrepancies show that satisfactory understanding of the energetics must await both more complete observations and a non-hydrostatic model with high resolution compared to the scale of the canyon. Closing energy budgets in models is further complicated by production changes accompanying pressure perturbations within the local domain produced by low-mode internal tides from distant sources [*Hall and Carter*, 2010].

7. Summary and discussion

Ascension Canyon is relatively short, with one 50° bend. Both its thalweg and its sides are mostly super-critical for M_2 internal tides. For comparison, Monterey Canyon is much longer, has several bends sharper than Ascension's, and is less steep, both along its sides and its thalweg, which is close to critical. Observations with an ADCP mounted on the bottom, microstructure profilers, and a depth-cycling towed body were compared with multiple model runs of a modified version of POM having 250-m resolution over a large domain. POM runs with and without Ascension in the bathymetry showed that its effect on barotropic tidal currents is large over the canyon and negligible beyond several kilometers. Runs with the canyon predicted accurately the tidal heights measured at the canyon's head with the ADCP but underestimated baroclinic currents significantly, likely because the spatial resolution needed to span the full domain did not resolve adequately small canyons like Ascension. Specific findings are:

1. Seaward of 4.5 km, average observed baroclinic energy densities matched the ratio expected for free, single ω_{M_2} waves, $hke/pe = 2.21$ [*Alford and Zhao*, 2007], but the observed ratio fell to landward around the bend as pe increased while hke decreased. Vertically-averaged baroclinic energy fluxes had magnitudes $\leq 300\ \mathrm{W\,m^{-1}}$ where the full water column was measured, but increased to seaward, even though depths below 650 m were not measured. Using observed dissipation rates, temporal changes in energy density,

and along-canyon divergences of the baroclinic flux, rough energy balances were computed, treating baroclinic production as a residual. These indicate both barotropic-to-baroclinic (positive) and baroclinic-to-barotropic (negative) production, governed mostly by along-canyon flux divergences and convergences and modulated by temporal changes in energy storage. Turbulent dissipation was usually, but not always, unimportant. The POM simulations treated dissipation as the residual and found it to be the most important term. Because both budgets, observed and modeled, produce large residuals, most likely neither is accurate. Both should be taken as preliminary, based on limited measurements and a numerical grid large relative to the canyon.

2. In the lowest 200 m, average dissipation rates decreased exponentially with height from 5×10^{-5} W kg^{-1} at the bottom and were 2–5 times smaller than the Monterey average. Decreasing from $K_\rho \approx 10^{-2}$ m^2 s^{-1} at the bottom to $\approx 10^{-3}$ at 200 m, owing to weaker stratification, diapycnal diffusivity equalled or exceeded Monterey in some places and was elsewhere within a factor of 2. This comparison, however, underestimates the true difference, because the Monterey data spanned a full spring–neap tidal cycle, whereas those in Ascension were obtained near spring tide. POM dissipation estimates were half those observed.

3. Beginning at 5 km, the most intense mixing patch extended 200 m up from the bottom and thinned around the bend, ending near 2.5 km. The turbulence appeared related to a layer of dense water pushed up along the bottom from deeper isotherms, suggesting that the mixing was related to internal bores like those found in Monterey [*Key*, 1999]. Because this patch dominated vertical averages, its thinning caused the

average to decrease toward the canyon head and around the bend. Similar decreases in dissipation around bends were observed in Monterey Canyon [*Kunze et al.*, 2002]. Smaller, but equally intense, mixing patches lay in a weakly stratified layer at the canyon top, tracking the rim as it slopes downward to seaward. Lee waves or rotors produced by steady flow across the canyon are possible causes of the mixing, but beams of the internal tide are also possible. Dissipation in Monterey was also most intense near the bottom, and internal bores were documented [*Key*, 1999], with some direct linkage to dissipation [*Carter and Gregg*, 2002].

Turbulence has been sampled in too few canyons to determine where Ascension fits among them, but its super-critical thalweg and the lack of strong tidal sources offshore should put it among the weaker members, as confirmed by these observations. Even so, because diapycnal diffusivity in the canyon is very high compared to levels outside the canyon, it is reasonable to assume that all canyons contain intense mixing.

In attempting energy balances, both observations, with inadequate temporal sampling, and model simulations, with inadequate spatial resolution, were pushed hard, perhaps too hard, but that is the direction future work should go; only when accurate energy budgets are obtained will we adequately understand canyon processes.

Acknowledgments. The National Science Foundation supported this work with grants OCE0751420 at the University of Washington and OCE0751226 at the University of Hawai'i. We are indebted to Captain Rick Verlini of R/V *Wecoma* and his officers and crew for their skill, forbearance, and good humor in making these results possible. Special thanks are also due to Daryl Swenson, Superintendent of O.S.U. marine technicians, for extensive and skillful help on deck. Jack Miller, John Mickett, Steve Bayer, Kim

Martini, Andrew Cookson, Paul Aguilar, and Keith Magness prepared and serviced our instruments and kept them from harm during nearly continuous close approaches to the bottom. Two annonomyous reviewers gave helpful comments that improved this report.

References

Alford, M., and Z. Zhao (2007), Global patterns of low-mode internal-wave propagation. Part II: group velocity, *J. Phys. Oceanogr.*, *37*, 1849–1858.

Carter, G., and M. Gregg (2002), Intense, variable mixing near the head of Monterey submarine canyon, *J. Phys. Oceanogr.*, *32*, 3145–3165.

Carter, G. S. (2010), Barotropic and baroclinic M_2 tides in the Monterey Bay region, *J. Phys. Oceanogr.*, *40*, 1744–1783.

Dillon, T. M. (1982), Vertical overturns: A comparison of Thorpe and Ozmidov length scales, *J. Geophys. Res.*, *87*, 9601–9613.

Egbert, G. (1997), Tidal data inversion: Interpolation and inference, *Progr. Oceanogr.*, *40*, 53–80.

Egbert, G., and S. Erofeeva (2002), Efficient inverse modeling of barotropic ocean tides, *J. Atmos. Ocean. Technol.*, *19*(2), 183–204.

Fofonoff, N. (1969), Spectral characteristics of internal waves in the ocean, *Deep-Sea Res.*, *16 (Suppl.)*, 58–71.

Garrett, C. J. R., and W. H. Munk (1975), Space-time scales of internal waves: A progress report, *J. Geophys. Res.*, *80*, 291–297.

Gordon, R., and N. Marshall (1979), Submarine canyons: Internal wave traps?, *Geophys. Res. Lett.*, *3*, 622–624.

Gregg, M., G. Carter, and E. Kunze (2005), Corrections to mixing rates in two papers about Monterey Submarine Canyon, Carter and Gregg (2002) and Kunze et al. (2002), *J. Phys. Oceanogr.*, *35*, 1712–1714.

Hall, R., and G. Carter (2010), Internal tides in the Monterey submarine canyon, *J. Phys. Oceanogr.*, *in press*.

Hotchkiss, F. S., and C. Wunsch (1982), Internal waves in Hudson Canyon with possible geological implications, *Deep-Sea Res.*, *29*, 415–442.

Jachec, S., O. Fringer, M. Gerritsen, and R. Street (2006), Numerical simulation of the internal tides and the resulting energetics with Monterey Bay and surrounding area, *Geophys. Res. Lett.*, *33*(L12605), doi:10.1029/2006GL026,314.

Key, S. (1999), Internal tidal bores in the Monterey Canyon, Ms, Naval Postgrad. School, Monterey, CA 93943-5000.

Klymak, J., M. Alford, R. Pinkel, R.-C. Lien, Y. Yang, and T. Tang (2010), The breaking and scattering of the internal tide on a continental slope, *J. Phys. Oceanogr.*, *submitted*.

Kunze, E., L. Rosenfeld, G. Carter, and M. Gregg (2002), Internal waves in Monterey Submarine Canyon, *J. Phys. Oceanogr.*, *32*, 1890–1913.

Lee, I.-H., R.-C. Lien, J. Liu, and W. s Chuang (2009a), Turbulent mixing and internal tides in Gaoping (Kaoping) Submarine Canyon, Taiwan, *J. Mar. Syst.*, *76*, 383–396.

Lee, I.-H., Y.-H. Wang, J. Liu, W.-S. Chuang, and J. Xu (2009b), Internal tidal currents in the Gaoping (Kaoping) Submarine Canyon, *J. Mar. Syst.*, *86*, 397–404.

Levine, M. (2002), A modification of the Garrett-Munk internal wave spectrum, *J. Phys. Oceanogr.*, *32*, 3166–3181.

Nash, J., M. Alford, and E. Kunze (2005), Estimating internal wave energy fluxes in the ocean, *J. Atmos. Ocean. Tech.*, *22*, 1551–1570.

Nash, J., E. Kunze, C. M. Lee, and T. B. Sanford (2006), Structure of the baroclinic tide generated at Kaena Ridge, Hawaii, *J. Phys. Oceanogr.*, *36*.

Niwa, Y., and T. Hibiya (2001), Numerical study of the spatial distribution of numerical study of the spatial distribution of the M_2 internal tide in the Pacific ocean, *J. Geophys. Res.*, *106*, 22,441–11,449.

Ozmidov, R. (1965), On the turbulent exchange in a stably stratified ocean, *Izvestiya, Atmos. Ocean Physics*, *1*(8), 853–860.

Percival, D., and A. Walden (1993), *Spectral Analysis for Physical Applications*, 583 pp., Cambridge Univ. Press, Cambridge, U.K.

Petruncio, E., J. Paduan, and L. Rosenfeld (2002), Numerical simulations of the internal tide in a submarine canyon, *Ocean Modelling*, *4*, 221–248.

Pratt, L., H. Deese, S. Murray, and W. Johns (2000), Continuous dynamical modes in straits having arbitrary cross sections, with applications to the Bab al Mandab, *J. Phys. Oceanogr.*, *30*, 2515–2534.

Thorpe, S. (1977), Turbulence and mixing in a Scottish loch, *Proc. Roy. Soc. Lond. A*, *286*, 125–181.

Wunsch, C., and S. Webb (1979), The climatology of deep ocean internal waves, *J. Phys. Oceanogr.*, *9*, 235–243.

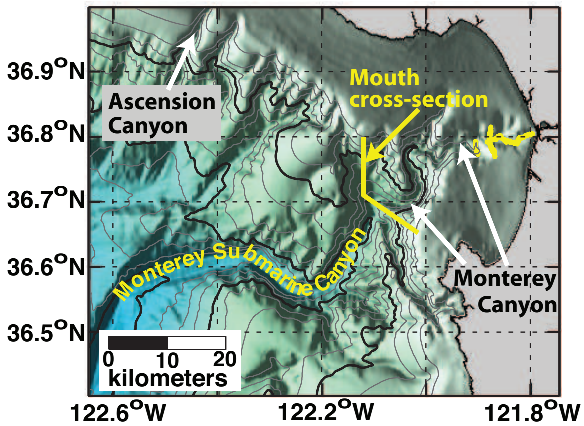

Figure 1. Bathymetry of Monterey Bay including Ascension and Monterey canyons. Yellow shading over the shallow end of Monterey Canyon was the region measured by *Carter and Gregg* [2002]. Internal tide fluxes entering Monterey Canyon from seaward were summed over the cross-section line.

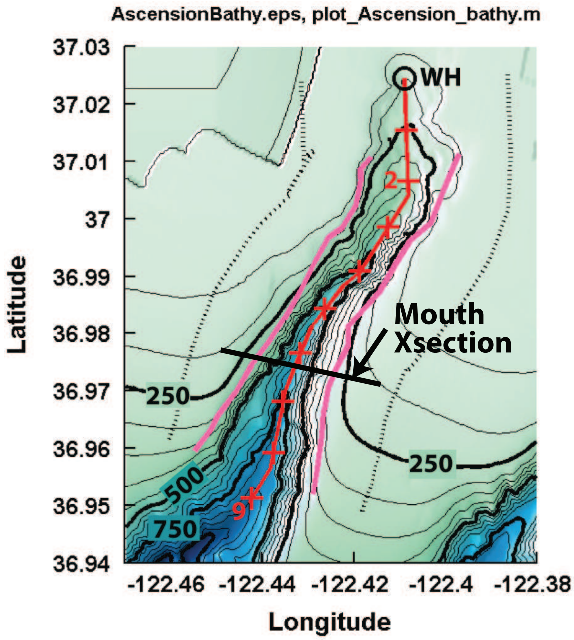

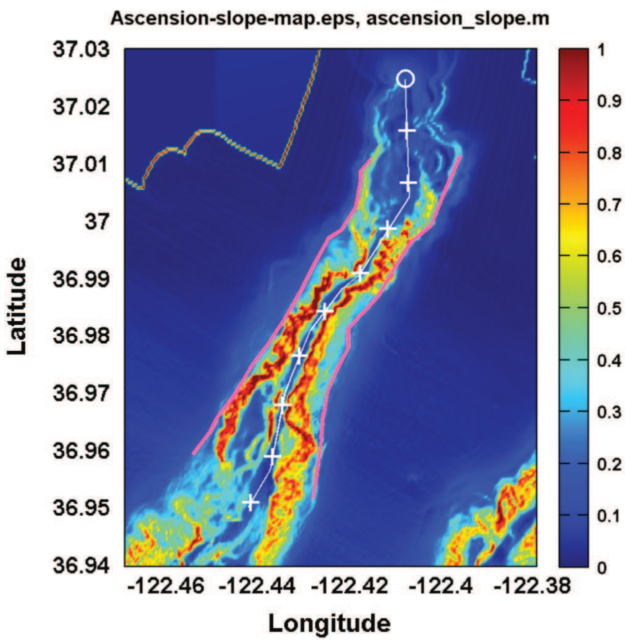

Figure 2. Depths (upper) and slopes (lower) of Ascension Canyon, based on 25-m bathymetry contoured at 50-m intervals. Circles mark the location of the 300-kHz WorkHorse ADCP, at the head of the thalweg, which is marked at 1-km intervals from the 200-m isobath. Dotted lines on the upper panel, 2 km either side of the thalweg, indicate the upper rim, where the shelf begins sloping downward toward the canyon. Pink lines mark the lower rim, where the slope first rises to 0.25. Ano Neuvo Canyon is at the lower right. Internal tide fluxes entering the canyon from seaward were summed over the cross-section line.

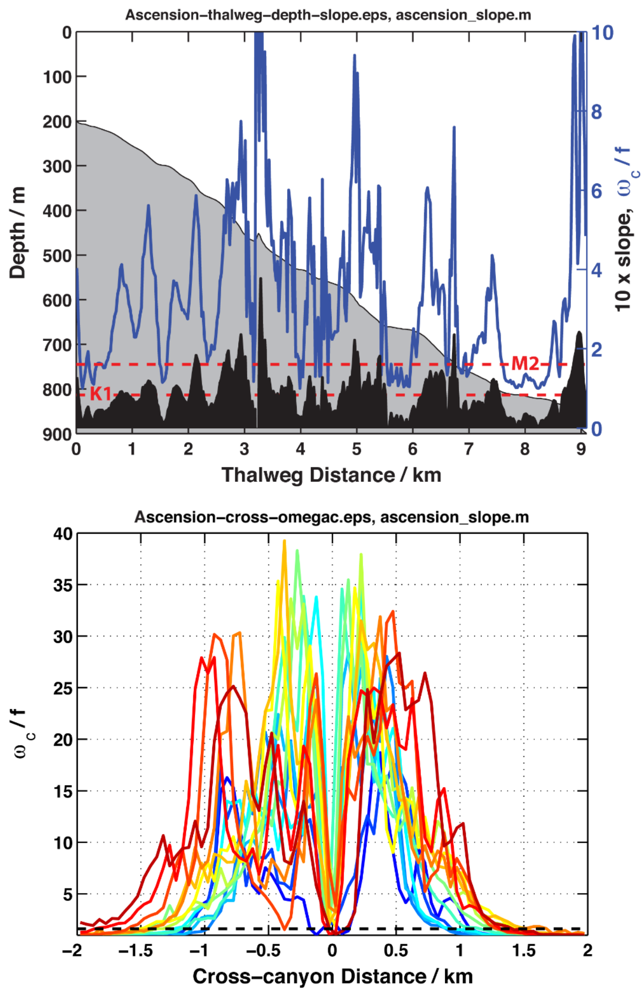

Figure 3. Upper) Thalweg characteristics: depth (shaded), slope (black), and critical frequency divided by the inertial frequency, f, (blue). Dashed red lines mark ω_c/f for K_1 and M_2 internal tides. Most of the thalweg has strongly supercritical slopes to K_1 and M_2, but some regions are slightly subcritical to M_2 and supercritical to K_1. Lower) Cross-canyon slopes at 0.5-km intervals along the thalweg, colored from blue at thalweg distance 1.5 km to red at 9 km. The dashed line marks the critical frequency for M_2. Critical slopes occur near the top of the sides, where the canyon blends into the shelf and continental slope.

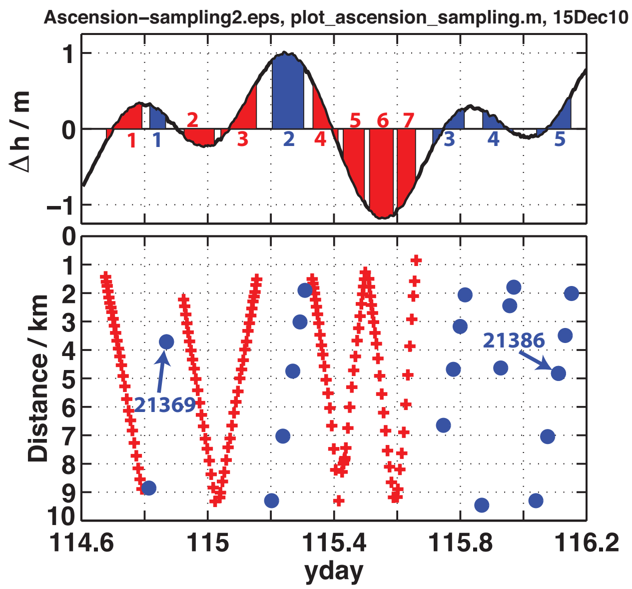

Figure 4. Upper) Tidal height fluctuations at Monterey pier during spring tide sampling in Ascension Canyon. Subs, i.e., individual runs in one direction, of SWIMS group 18 are red, and those of AMP group 7 are blue. Both sets are numbered sequentially. Lower) Times and distances of each SWIMS and AMP profile. (yday began with 0.0 at midnight on 31 December 2008.) SWIMS sub 1 is plotted in Figure 13, and AMP 21369 and 21386 are plotted in Figures 15 and 12, respectively.

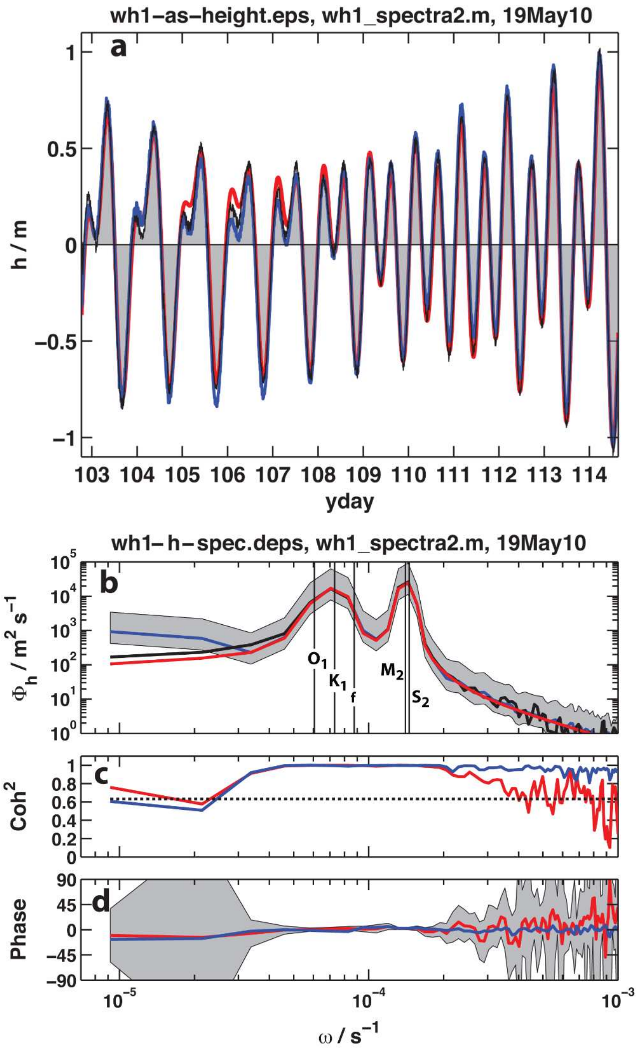

Figure 5. a) Sea level fluctuations at the head of Ascension Canyon: observed with the WorkHorse ADCP (shading bounded by black line), observed at Monterey pier (blue), and predicted by POM forced with eight tidal constituents (red). b) Amplitude spectra of height fluctuation with the same colors for the three records. Tidal constituents are shown for reference, but the time series is too short for the spectral window to resolve closely-spaced frequencies, e.g., K_1 and O_1. c) Coherence spectra between Ascension and Monterey observations (red) and between POM simulation at the WorkHorse ADCP and Monterey observations (blue). Dotted line is the 95% confidence level for significant coherence. d) Phase for the same pairs as in c. These and following spectra were computed with multitapers using three Riedel weights [*Percival and Walden*, 1993].

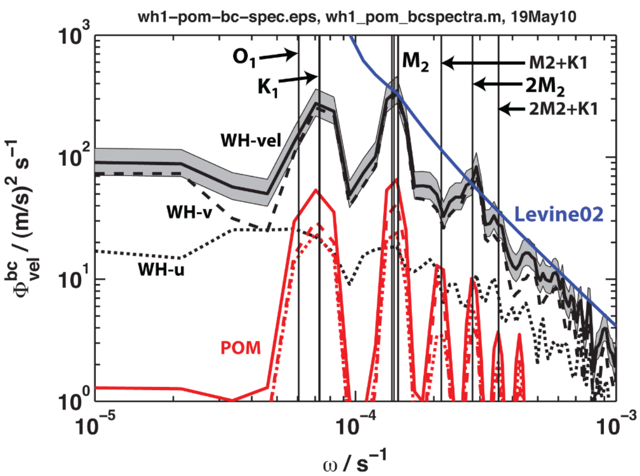

Figure 6. Vertical averages of baroclinic spectra computed for each Workhorse depth bin below the rim (black), and model over the full-depth (red), including total velocity (solid), u (dots), and v (dashes). The *Levine* [2002] shallow water spectrum evaluated for stratification and depth in the canyon is blue. It was calculated with $j_* = 3$ and energy density equal to *Garrett and Munk* [1975]. Shading gives 95% confidence limits for the WH1 velocity spectrum, i.e., the sum of u and v spectra.

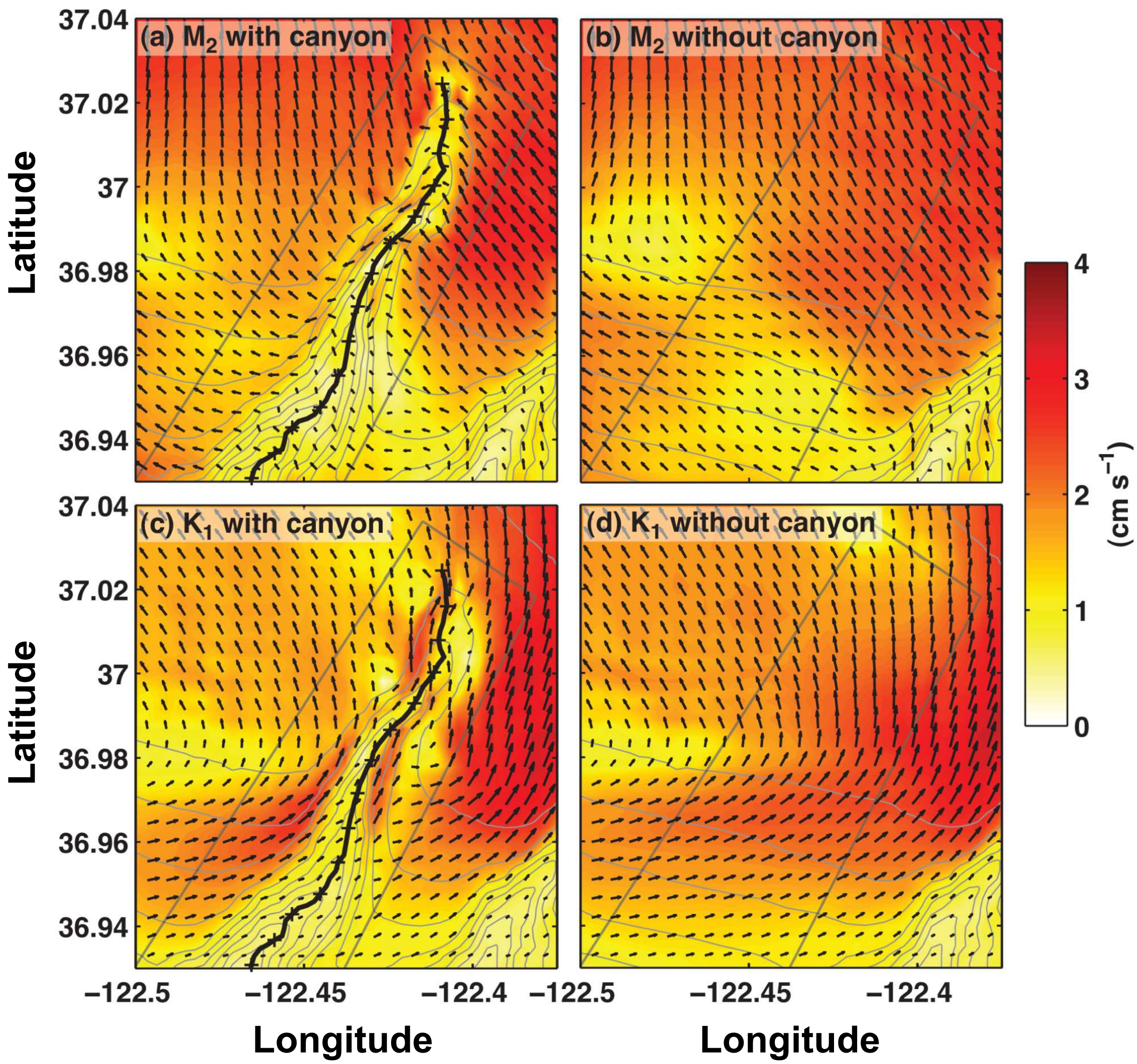

Figure 7. Barotropic tidal currents during flood tide at every second grid point used by the POM high-resolution primitive equation model [*Hall and Carter*, 2010] with M_2-only tidal forcing (top panel) and K_1-only forcing (lower panel). Solid straight lines bound bathymetry removed to compare tidal currents with and without Ascension Canyon, demonstrating a large perturbation over and very near the canyon. The perturbation caused by Ano Neuvo Canyon, lower right, is also large, and did not change when Ascension was removed. The flow was estimated for 1.5 hours before high water. The thick solid line on the left is the thalweg, deepest path, of Ascension Canyon, marked at 1-km intervals.

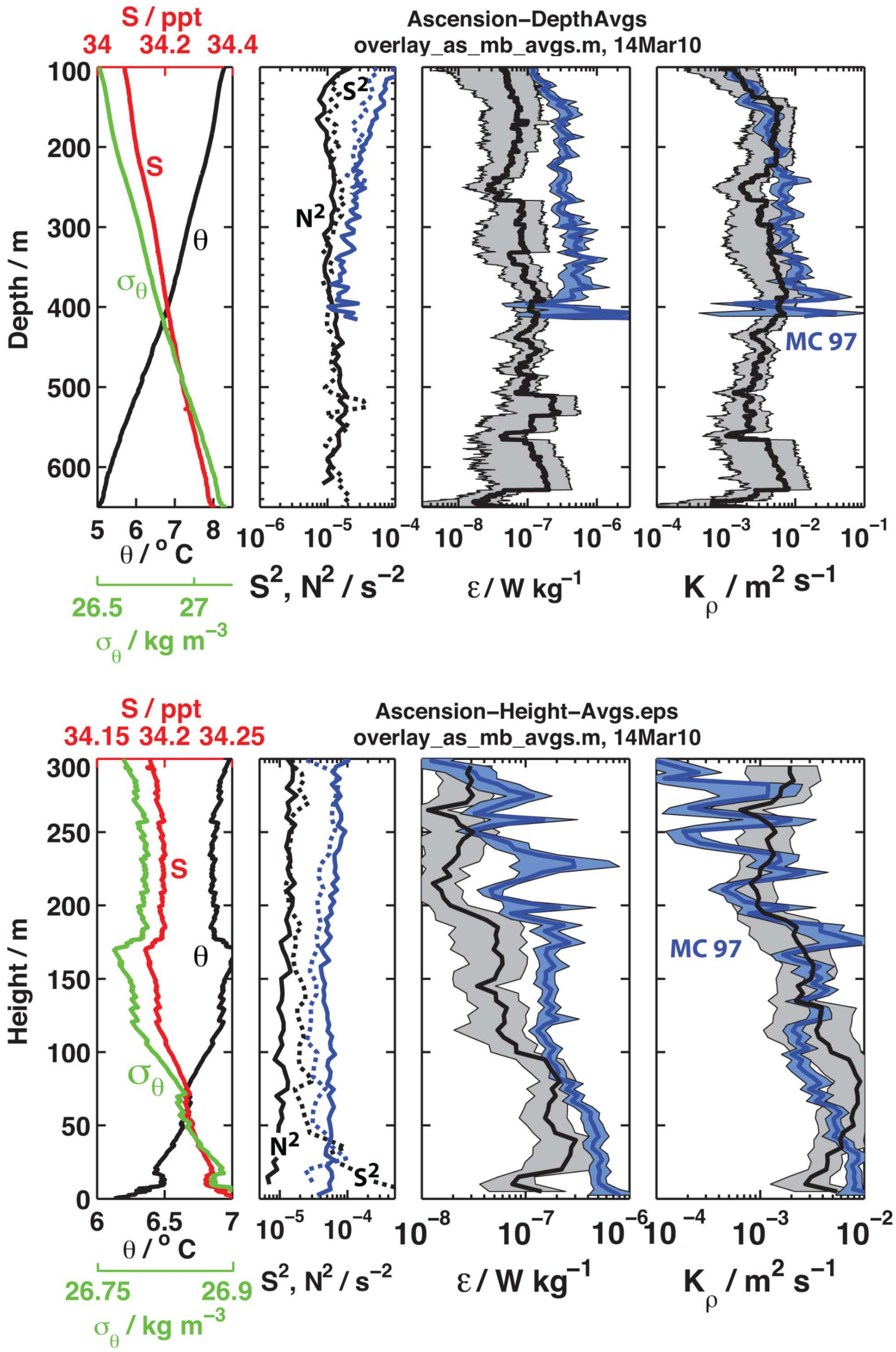

Figure 8. Ascension averages, compared in the three panels to the right with Monterey averages (blue) observed during 1997 [*Carter and Gregg*, 2002; *Gregg et al.*, 2005]. The upper set are plotted versus depth and the lower set against height above the bottom. For both canyons, S^2 (dashed) substantially exceeds N^2 (solid) near the bottom. Only data below the canyon rim were used for the height averages.

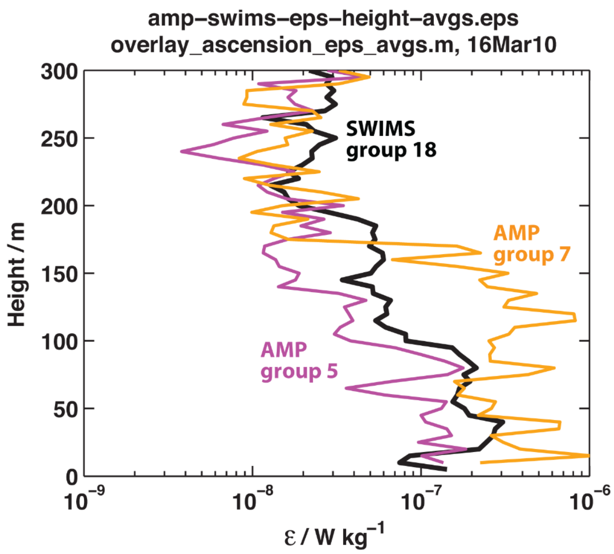

Figure 9. Averages of all AMP and SWIMS profiles in Ascension Canyon, including only data below the rim, plotted versus height above the sea floor. Taken during neap tides, AMP group 5 was smaller than SWIMS3 group 18 and AMP group 7 below $h = 175$ m. SWIMS3 group 18 and AMP group 7 were taken at spring tide.

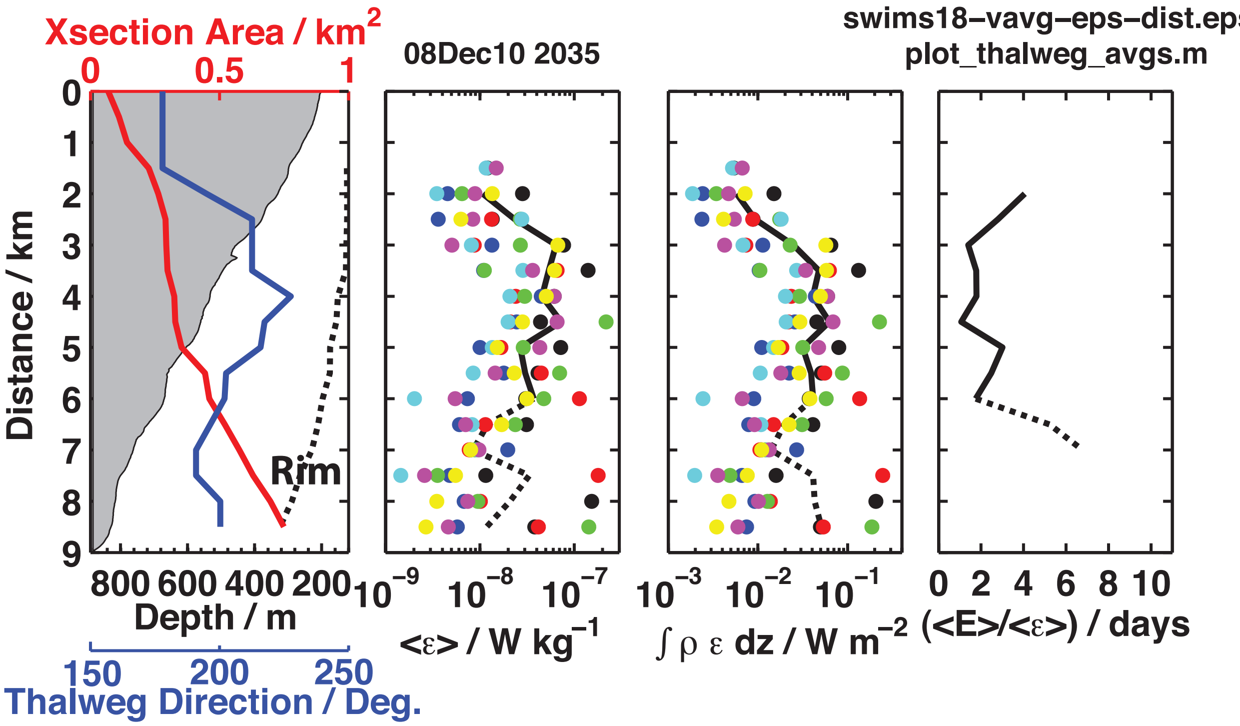

Figure 10. a) Canyon characteristics: depth (shaded), upper rim depth (dotted), cross-sectional area (red), and direction going seaward (blue). b) Dots are vertically averaged ϵ for each sub of SWIMS group 18 (Figure 4) at each position along the thalweg. In sequence, subs 1–7 are black, red, blue, green, cyan, maroon, and yellow. The line is the group average. It and other lines are dotted at the seaward end, where profiles did not reach the bottom. c) Vertically integrated ϵ in the same format as panel b. d) Total energy divided by average dissipation rate, yielding estimates of energy decay times.

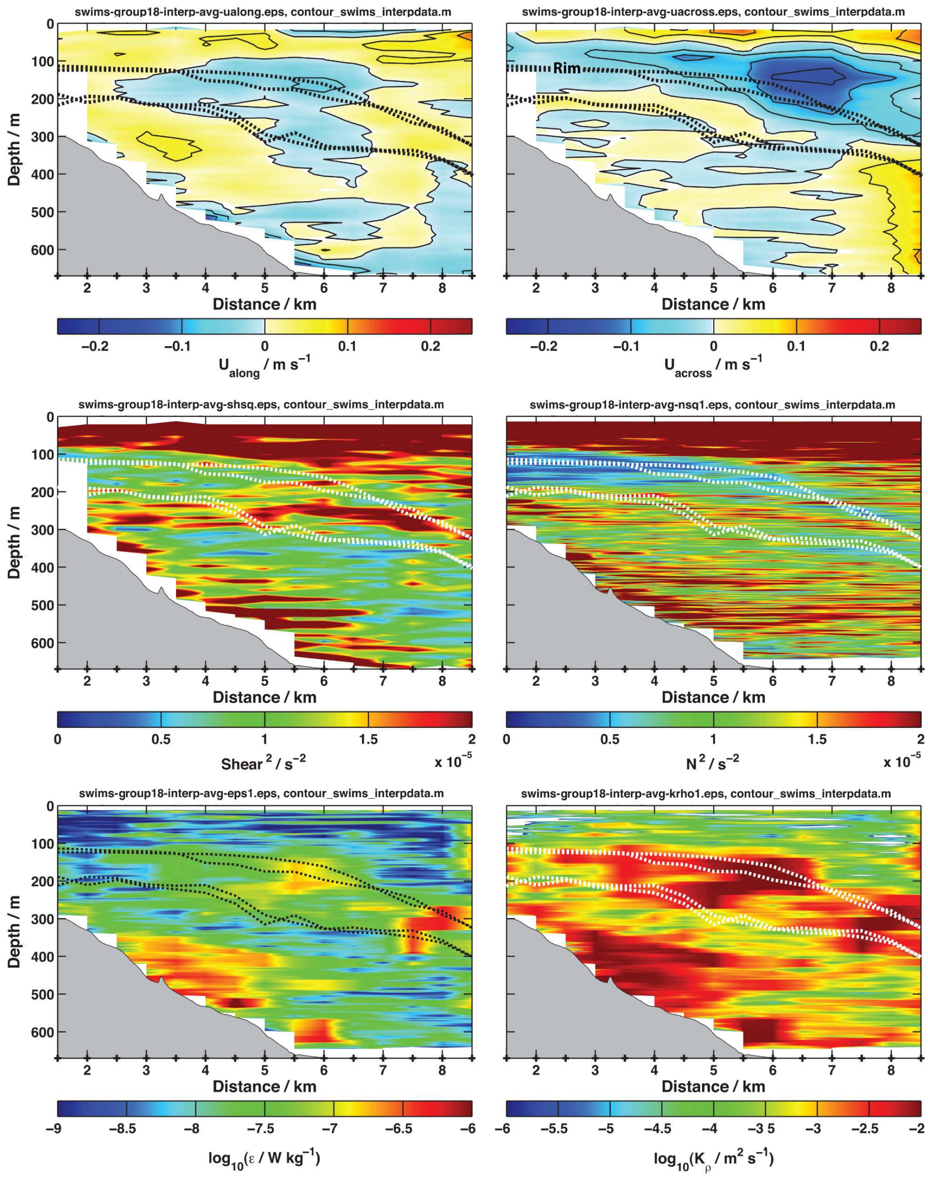

Figure 11. Averages of all SWIMS3 subs after interpolation onto a 5-m by 0.5-km grid. In this and similar figures, variable labels and color bars are below data plots. U_{along} and U_{across} are positive toward the head and east side of the canyon (right side facing toward the head). Dotted lines show depths of upper and lower rims.

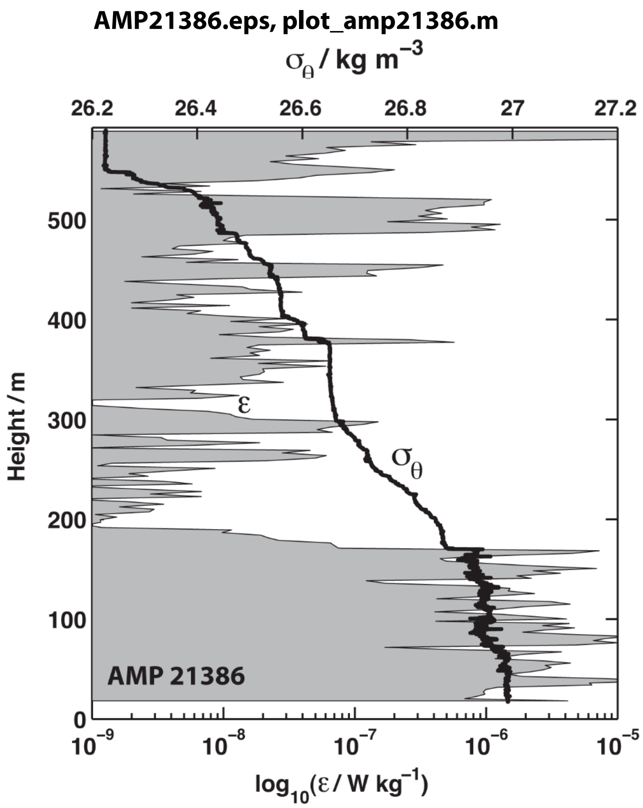

Figure 12. AMP21386, taken at 4.83 km on the thalweg on yday=116.1108. Heights begin at the bottom, determined with an acoustic altimeter. Intense turbulence in the bottom 200 m spans a 50-m-thick homogenous bottom boundary layer capped by 150 m of overturning stratified water.

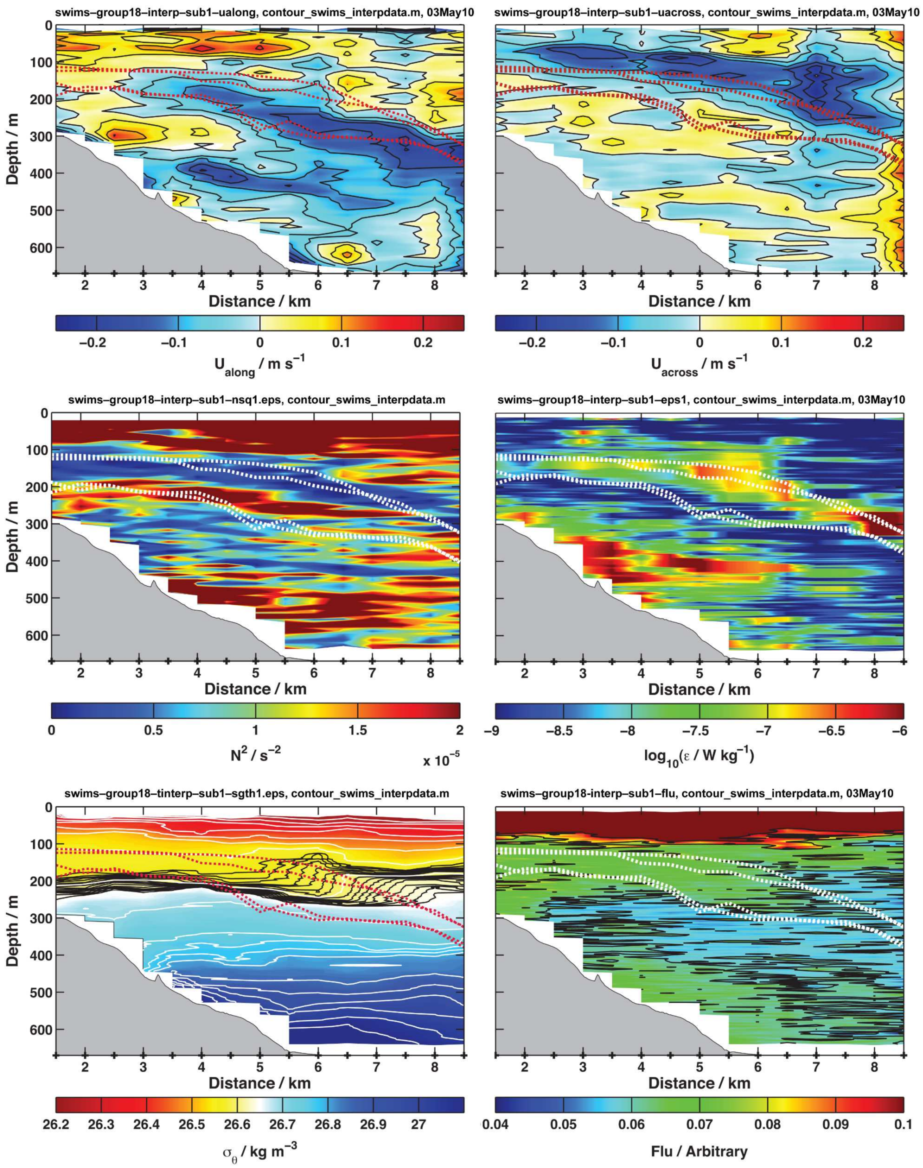

Figure 13. SWIMS3 sub 1. The well-mixed layer between the rims extended nearly to the end of the section and was flowing out of the canyon. The vertical displacement of isopycnals between 3 and 5 km at the bottom relative to their offshore depth indicates that the dense water had run 1.5 km up the thalweg, most likely as a bore. The deepest flow was still moving shoreward, possibly accounting for the intense turbulence at the feature's head. Isopycnal overlays change color as needed to stand out against the background.

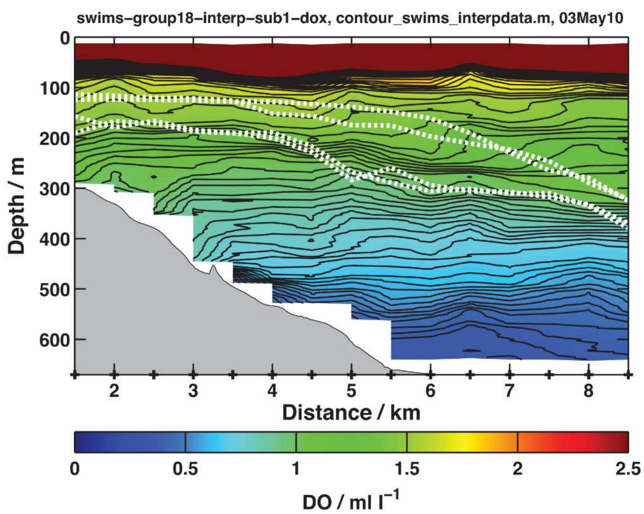

Figure 14. Concentration of dissolved oxygen during SWIMS3 group 18, sub 1, showing low-oxygen water pushed up the bottom between 5.5 and 3.5 km, bounded by nearly vertical contours farther upslope.

AMP21369.eps, plot_amp21369.m

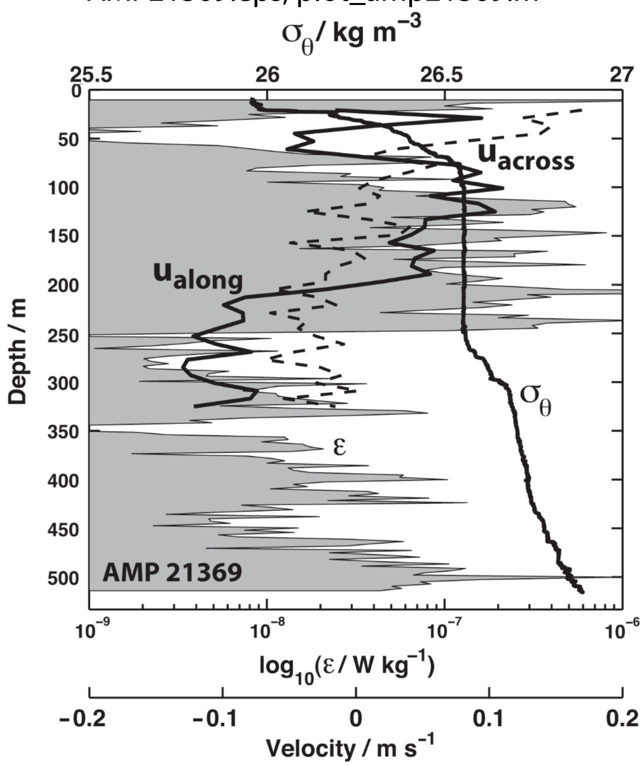

Figure 15. AMP21369, taken at 3.72 km on yday=114.8700, sampled a 200-m-thick, well-mixed layer of intense turbulence, most of which was flowing toward the canyon's head. Along-thalweg velocity was obtained with the ship's 75-kHz ADCP.

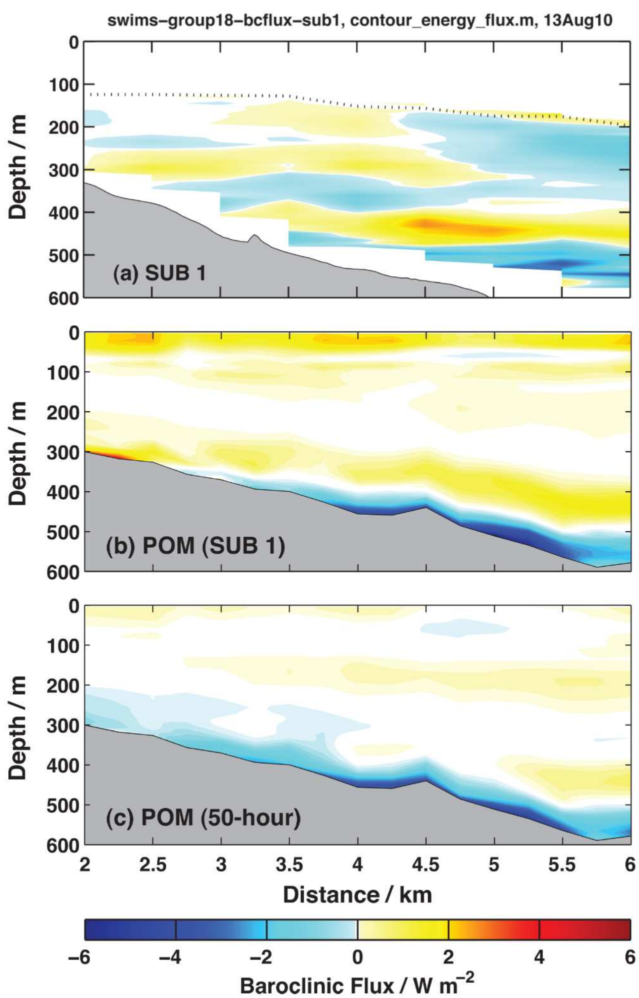

Figure 16. Baroclinic flux within the canyon for SWIMS sub 1, positive toward the head. Upper) Along-thalweg flux observed with SWIMS3, Middle) Along-thalweg flux from POM simulation averaged over the ≈ 4-hour period corresponding to sub 1, Lower) Along-thalweg flux from POM averaged over 50 hours centered on sub 1.

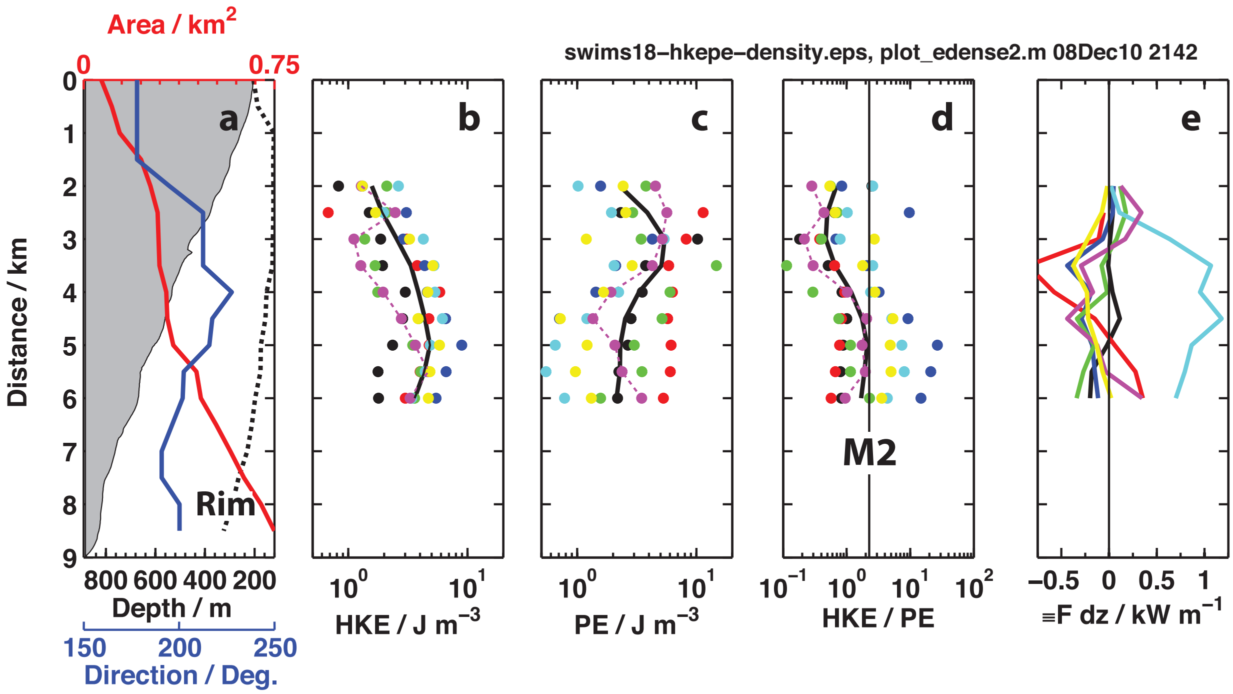

Figure 17. Vertical averages of horizontal kinetic and potential baroclinic energy densities, their ratio, and total along-thalweg energy fluxes. Thick solid curves in panels b, c, and d are time averages; colored dots as in Figure 10. In panel d, the straight vertical line marks the *hke*/*pe* ratio expected for the M_2 internal tide. Dot colors are the same as in Figure 10. Dashed lines connect maroon dots of sub 6.

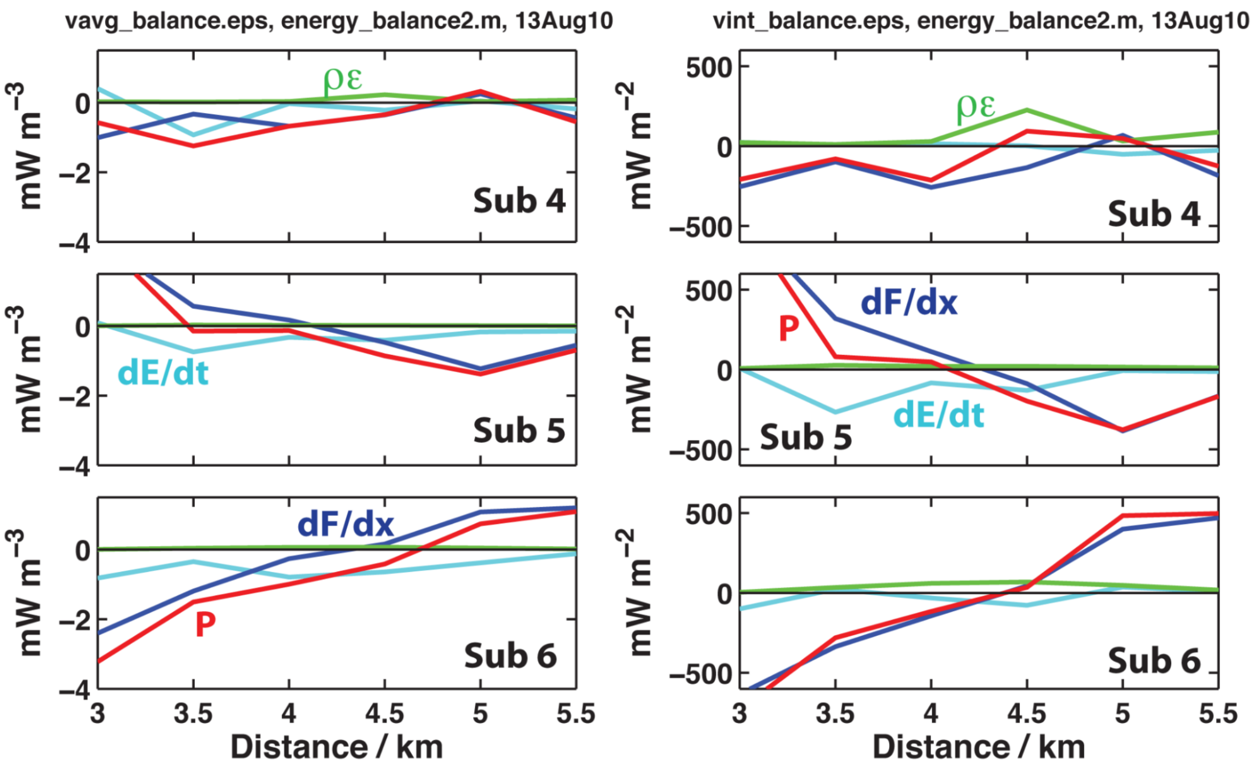

Figure 18. Evaluation of the energy budget (Eq. 2) using vertical averages (left) and vertical integrals (right) of measurements along the thalweg, with production, P, computed as a residual of the three measured terms. Flux divergence, dF/dx, was usually the largest and turbulent dissipation, $\rho\epsilon$, the smallest term, but changes in energy density, dE/dt, were sometimes important. The tide changed from maximum ebb during sub 4 to low water during sub 6.

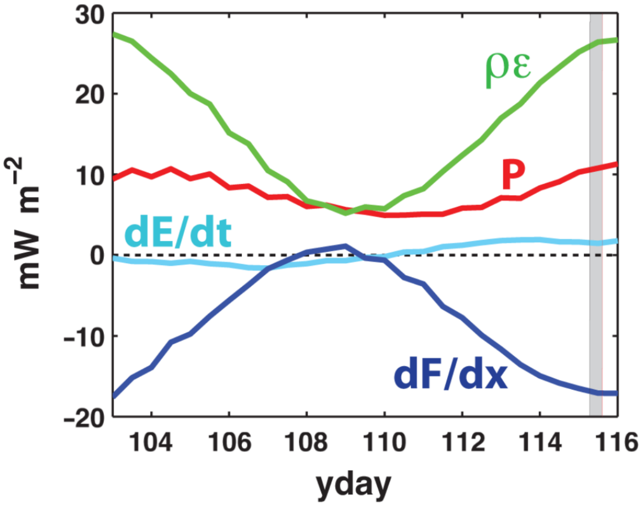

Figure 19. Evaluation of the energy budget (Eq. 2) obtained with the POM model, represented as a 25-hr moving window and integrated over the upper canyon area. The vertical gray band marks when budgets were estimated with SWIMS3 data (Figure 18).

Table 1. Comparison of physical characteristics, baroclinic energy fluxes, F_E, and mixing in Ascension and Monterey canyons. Unless otherwise noted, fluxes and mixing rates were computed using POM. Separate simulations forced Ascension with eight tidal constituents and with only the M_2 constituent. Monterey was forced only with M_2, as reported by *Hall and Carter* [2010]. Lines in Figures 1 and 2 show locations of lines used for mouths of the canyons. Fluxes are positive into the canyons, and fluxes impinging on Ascension are based on calculations over the wide domain shown in Figure 11 of *Hall and Carter* [2010]. The average dissipation rate in Monterey was observed in the upper canyon during MC97 and restated by *Gregg et al.* [2005].

Parameter	Ascension		Monterey
Maximum width (km), depth (m)	3.2, 643		21.3, 1,858
Mouth-to-head distance (km)	7		51
Average cross-sectional area (km^2)	9.2		223.4
Volume (km^3)	2.98		186.55
Observed dissipation rate (W kg^{-1})	1.02×10^{-7}		1.97×10^{-7}
Observed K_ρ (m^2 s^{-1})	3.92×10^{-3}		2.5×10^{-3}
	eight constituents	M_2	M_2
$\left\langle \int F_E \, dz \right\rangle_x$ across mouth (Wm^{-1})	33.3	18.9	420
$\int F_E \, dxdz$ into mouth (kW)	115	65	9,023
$\int F_E \, dxdz$ across rim (kW)	–39	–11	–1,451
Flux convergence (kW)	76	54	7,572
Barotropic-to-baroclinic conversion (kW)	72	158	50
Dissipation rate (W kg^{-1})	4.85×10^{-8}	7.66×10^{-8}	3.99×10^{-8}

Table 2. Average dissipation rates in Ascension Canyon from AMP and SWIMS3, estimated using bootstrap with m=500 for data in 5-m bins. Upper and lower 95% confidence limits are ϵ_{ub} and ϵ_{lb}.

Data	ϵ_{lb}	$< \epsilon >$	ϵ_{ub}	Profiles
Monterey 97	2.75×10^{-7}	2.87×10^{-7}	3.00×10^{-7}	342
AMP group 5	3.87×10^{-8}	4.68×10^{-8}	5.88×10^{-8}	16
SWIMS group 18	1.04×10^{-7}	1.08×10^{-7}	1.12×10^{-7}	140
AMP group 7	1.55×10^{-7}	1.89×10^{-7}	2.36×10^{-7}	21